Article

Magnetic flux trapping in hydrogen-rich high-temperature superconductors

V. S. Minkov [1] ✉, V. Ksenofontov[1], S. L. Bud'ko [2,3], E. F. Talantsev [4,5] & M. I. Eremets [1] ✉

Recent discoveries of superconductivity in various hydrides at high pressures have shown that a critical temperature of superconductivity can reach near-room-temperature values. However, experimental studies are limited by high-pressure conditions, and electrical transport measurements have been the primary technique for detecting superconductivity in hydrides. Here we implement a non-conventional protocol for the magnetic measurements of superconductors in a SQUID magnetometer and probe the trapped magnetic flux in two near-room-temperature superconductors H_3S and LaH_{10} at high pressures. Contrary to traditional magnetic susceptibility measurements, the magnetic response from the trapped flux is almost unaffected by the background signal of the diamond anvil cell due to the absence of external magnetic fields. The behaviour of the trapped flux generated under zero-field-cooled and field-cooled conditions proves the existence of superconductivity in these materials. We reveal that the absence of a pronounced Meissner effect is associated with the very strong pinning of vortices inside the samples. This approach can also be a tool for studying multiphase samples or samples that have a low superconducting fraction at ambient pressure.

The current search for room-temperature superconductivity has progressed due to advances in high-pressure studies. A decade ago, superconductivity was assumed to be a solely low-temperature phenomenon with the highest superconducting critical temperature of $T_c \approx 130$ K found in mercury-containing[1] and thallium-containing[2] cuprate superconductors. The discovery of superconductivity in H_3S with T_c of approximately 200 K (ref. 3) suggested that T_c could be much higher in conventional superconductors for which the Bardeen–Cooper–Schrieffer theory[4–6] was established. Thereafter, T_c up to around 250 K was found in transition metal superhydrides YH_9 (ref. 7) and LaH_{10} (refs. 8–10). These experimental discoveries were anticipated by accurate theoretical predictions[11–13], which became feasible owing to the continuous development of ab initio methods for the prediction of crystal structure and computation of superconducting properties[14–16].

Although extreme pressure conditions render these record-high-T_c superconductors unsuitable for technological applications, the study of high-temperature superconductivity in various phases of hydrogen-rich compounds has highlighted the fundamental problem of the ultimate value of T_c possible in a superconductor. The latest theoretical predictions suggest that very high multi-megabar pressures are required for superconductivity above room temperature[17,18]. Another promising direction includes investigating effective methods for the stabilization of high-T_c phases at lower pressures, ideally at ambient conditions, for example, by doping[19–21]. The experimental hydrogenation of Y–La (ref. 22), La–Nd (ref. 23) and Ce–La (refs. 21,24) binary alloys was studied, but without a noticeable enhancement in T_c and pressure range of stability of presumably ternary final superhydrides compared with the parent binary Fm-$3m$-LaH_{10} and $P6_3/mmc$-LaH_{-9-10} phases[8].

[1]Max Planck Institute for Chemistry, Mainz, Germany. [2]Ames Laboratory, US Department of Energy, Iowa State University, Ames, IA, USA. [3]Department of Physics and Astronomy, Iowa State University, Ames, IA, USA. [4]M.N. Mikheev Institute of Metal Physics, Ural Branch of the Russian Academy of Sciences, Ekaterinburg, Russian Federation. [5]NANOTECH Centre, Ural Federal University, Ekaterinburg, Russian Federation. ✉e-mail: v.minkov@mpic.de; m.eremets@mpic.de

However, high pressures necessitate tiny micrometre-sized samples and drastically limit the available techniques for the experimental study of superconductivity. Electrical transport measurements have been successfully adopted in the multi-megabar pressure range and have become the primary technique to detect superconductivity[25–27]. They provide data on T_c, and the estimates of the upper critical magnetic field $\mu_0 H_{c2}$ and coherence length ξ of superconductors, as they are performed in high external magnetic fields. Other key parameters of superconductivity, such as the lower critical field H_{c1} and London penetration depth λ_L, can be obtained from magnetic susceptibility measurements. This type of measurement is crucial for understanding the complex behaviour of type-II superconductors in a magnetic field, particularly for the study of vortices.

Two techniques are currently used for magnetic measurements at high pressures: a double modulation a.c. technique with a system of coils[28], and a superconducting quantum interference device (SQUID)[29]. The first technique provides only a qualitative indication of the superconducting transition and is not widely distributed due to its complexity and low sensitivity[30,31]. Conversely, static d.c. measurements in the SQUID are simpler, and the results are well interpreted because they comprise absolute values of magnetic susceptibility. Initially, such measurements were limited to the order of 10 GPa, and the signal was severely distorted by the background of a bulky diamond anvil cell (DAC)[32,33]. The development of a miniature DAC[3,29] and recent improvements in background subtraction[34] have greatly extended the scope of the method.

Here we improved the studies of superconductors at high pressures by introducing the trapped flux method. This method is based on the detection of magnetic flux that originates from the conjunctive action of several properties and effects in superconductors (the persistent dissipation-free current flow, quantum split of magnetic field into Abrikosov vortices, the pinning of vortices by structural defects and so on) and traps in a sample after switching off an external magnetic field. These measurements have several advantages over typical magnetic susceptibility measurements, as they are performed in a zero magnetic field, and thus, the background signal from the DAC is cancelled. The signal from the trapped flux can be approximately one to two orders of magnitude higher than the response from the zero-field-cooled (ZFC) field-screened state at low magnetic fields, and therefore, substantially smaller samples can be studied. This method is particularly beneficial for the study of superconductors having large pinning (which has been observed in several recently discovered superconductors) and is effective at distinguishing between different phases in multiphase samples, probing critical current densities j_c in a wide temperature range and determining H_{c1}.

The Im-$3m$-H_3S sample showed a pronounced superconducting transition in ZFC $m(T)$ magnetization measurements with $T_c \approx 195$ K, 18 months after its synthesis (Fig. 1a). At lower temperatures, the sample underwent the second superconducting transition with $T_c \approx 15$ K (seen as a separation of the ZFC and field-cooled (FC) portions of the $m(T)$ data on the background of the DAC signal (Fig. 1b)). The detected low-temperature superconductivity most probably corresponded to elemental sulfur, which was extruded on the bevels of diamond anvils during the pressurization of the sandwiched sample of NH_3BH_3 + S and remained intact after the pulsed-laser-assisted synthesis (Fig. 1b, inset). The superconducting transition in sulfur was extended in the temperature range of 12–18 K, which could be attributed to the substantial pressure gradients on the beveled slope of the diamond anvils. The measured T_c was in good agreement with previous observations of superconductivity in sulfur at high pressures[30,35,36].

Trapped flux measurements

The magnetization of a type-II superconductor is irreversible due to the pinning of vortices if the superconductor contains defects, such as dislocations, precipitates and phase boundaries, which interact with the flux lines penetrating the superconductor above H_{c1}.

The temperature dependencies of the trapped magnetic moment $m_{trap}(T)$ generated in H_3S under ZFC and FC conditions at different H_M values and measured between 10 and 250 K at zero field clearly showed a superconducting transition with $T_c \approx 195$ K (Fig. 1c,d and Extended Data Figs. 1 and 2), further revealing a steep upturn below ~15 K, which originated from pure sulfur. The entry of magnetic flux into sulfur occurred at $\mu_0 H_M = 30.0$ mT in the ZFC mode and 0.5 mT in the FC mode, which were the lowest applied magnetic fields in the two runs. This indicated that metallic sulfur belonged to either type-II or dirty type-I superconductors[37,38]. To exclude the contribution of sulfur to the measured magnetic response, only a portion of the $m_{trap}(T)$ data collected above 30 K was used to interpret the temperature dependence of the trapped flux in H_3S.

In the FC mode, even weak applied magnetic fields as low as 0.5 mT resulted in a positive non-zero magnetic response of the trapped flux in H_3S (Fig. 2a). In this mode, the magnetic flux penetrated the sample in the normal state at $T > T_c$ and became trapped at $T < T_c$ due to very strong pinning (as discussed below).

Contrary to the FC mode, the ZFC magnetization provided valuable data for estimating H_p, when the applied magnetic field starts to penetrate the sample[39–41] (Fig. 1c). No trapped flux in ZFC H_3S was observed up to $\mu_0 H_M = 45$ mT. In this range, the external magnetic field was completely repelled from the H_3S phase. We estimated $\mu_0 H_p(10 \text{ K}) = 42 \pm 3$ mT from the data measured at $45 \leq H_M \leq 125$ mT (Fig. 1 and inset in Fig. 2a).

At higher H_M, the magnetic flux penetrated the superconductor from the outer edges of the disc-shaped sample and gradually propagated towards its centre. The entry of magnetic flux led to a reduction in the Meissner currents, and being trapped to the appearance of superconducting current loops and a corresponding increase in sample magnetization at zero field. The absence of steps in the $m_{trap}(H_M)$ data and smooth increase in m_{trap} with an increase in H_M implied the absence of a weak-link network in the superconducting sample[42].

The observed trapped magnetic moment in the superconducting Im-$3m$-H_3S phase saturated under the ZFC and FC conditions at different values of H_M. We qualitatively interpreted this behaviour of the magnetization process in terms of the classical critical-state Bean model[43,44] and considering the reversible part of magnetization in type-II superconductors[39,45]. According to the model, flux trapping saturates if the applied magnetic field reaches the value $H_M = 2H^* + H_p$ in the ZFC mode and $H_M = H^*$ in the FC mode, where H^* is the full penetration field (Fig. 2b).

The trapped magnetic moment became saturated (m_{trap}^s) at $\mu_0 H_M \approx 1.50$ T under ZFC conditions and at $\mu_0 H_M \approx 0.65$ T under FC conditions, and did not vary with a further increase in $\mu_0 H_M$ up to 6.00 T (Figs. 1c,d and 2a). Thus, $\mu_0 H^* = 700 \pm 50$ mT. The observed saturation is defined by the maximum value of the trapped magnetic field in the sample and corresponds to the in-field critical current density $j_c(B,T)$ and density of pinning centres in the superconductor.

We also estimated H_{c1}, which is proportional to H_p using the relation $H_{c1} = \frac{1}{1-N} H_p$. We used the same estimations for the size of samples and demagnetization factor N as in another work[34]. Using the estimated demagnetization correction of 8.5 (although it could range between 7.7 and 11.4; Methods), $\mu_0 H_{c1}(10 \text{ K}) \approx 0.36$ T (0.32–0.48 T).

The obtained value of $\mu_0 H_p \approx 42$ mT was noticeably lower than that derived from the virgin curves of hysteretic magnetization loops (≈ 95 mT) in classical $m(H)$ measurements[29,34]. We considered the trapped flux method to be more sensitive to the determination of the onset of magnetic flux entry because a large linear contribution of the initial portion of $m(H)$ was cancelled. The advantage of this method for type-II superconductors having strong pinning was illustrated in another work[45]. Additionally, the signal of the trapped magnetic moment at zero field does not contain the field-dependent magnetic background arising from the DAC, which is unavoidable in classical
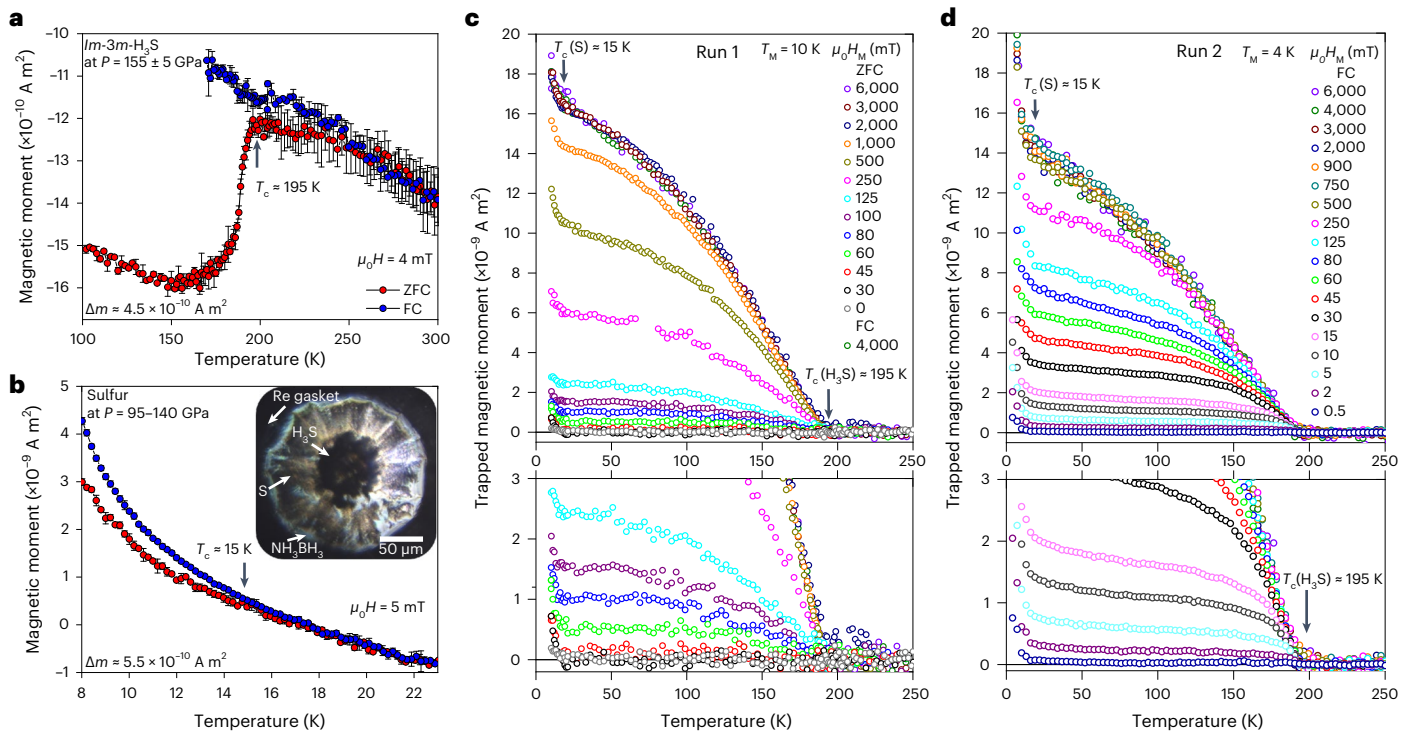
Fig. 1 | Magnetic measurements of sample containing H_3S and elemental sulfur. a, ZFC and FC $m(T)$ data of Im-$3m$-H_3S at 155 ± 5 GPa. **b**, ZFC and FC $m(T)$ data of sulfur at 95–140 GPa. The error bars represent the standard deviation from multiple measurements. The inset shows a photograph of the sample and the spatial distribution of H_3S and S. **c,d**, Temperature dependence of a trapped magnetic moment at zero field generated under ZFC (run 1; **c**) and FC (run 2; **d**) conditions. The open circles of different colours correspond to the temperature dependence of the trapped flux created at different magnetic fields $\mu_0 H_M$ (0–6 T). The lower panels reveal the beginning of the penetration of flux lines into the H_3S sample above $\mu_0 H_M = 45.0$ mT (run 1) and already at $\mu_0 H_M = 0.5$ mT (run 2).
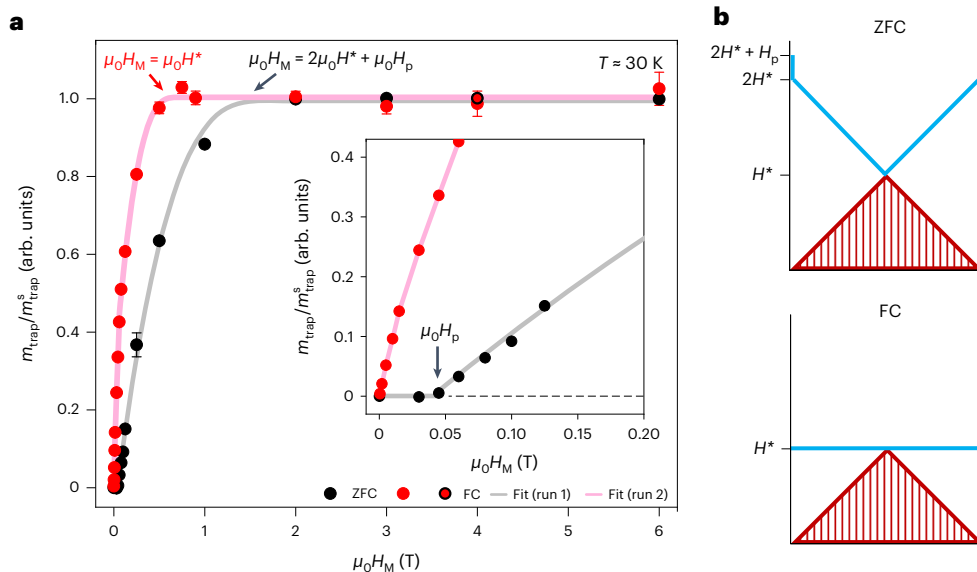

Fig. 2 | Trapped magnetic moment in Im-$3m$-H_3S sample at 30 K. a, Dependence of a trapped magnetic moment at zero field on magnetization field $\mu_0 H_M$ measured in the ZFC and FC modes (runs 1 and 2). The circles correspond to the experimental data, and the magenta and grey curves are guides for the eye. The trapped flux was created in the ZFC (black circles) and FC (red circle) modes at several applied magnetic fields H_M. The inset with the enlarged plot shows the entry of the magnetic field into the sample at low H_M. The error bars represent uncertainties in the estimation of values of m_{trap}/m_{trap}^s. **b**, Profile of magnetic field in the disc-shaped sample in applied magnetic field $H_M = 2H^* + H_p$ (ZFC mode) and $H_M = H^*$ (FC mode) (area below the blue lines) and after removing the applied magnetic field (hatched red area).

$m(H)$ magnetization measurements. It should be noted that the presence of tiny, fragmented parts of the superconducting phase and the ragged edges of the bulky sintered sample (Fig. 1b, inset) could influence the observed H_p. The contribution of these imperfections to the total measured magnetic moment was almost negligible in $m(H)$ experiments because the magnetic flux penetrated these areas at substantially low applied magnetic fields due to the extremely large demagnetization factor. In the trapped flux method, these areas
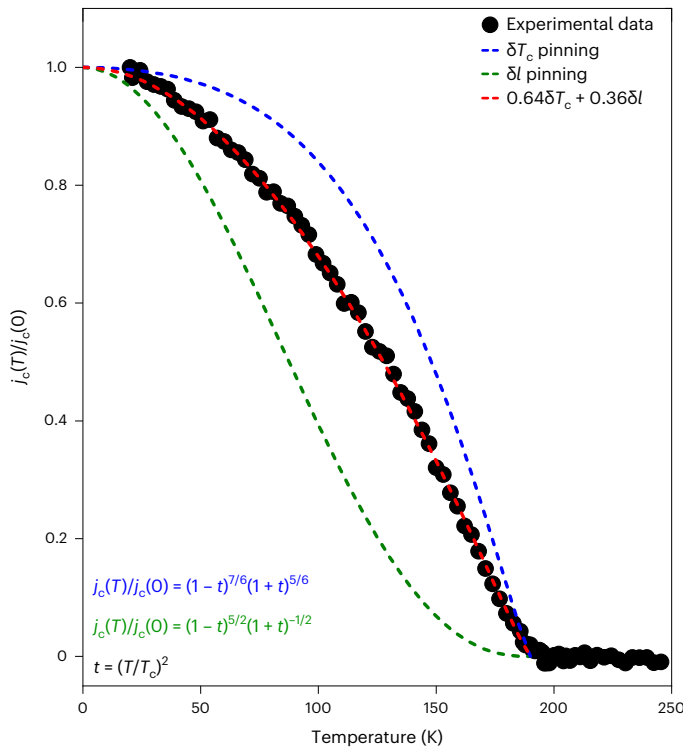
Fig. 3 | Temperature dependence of the normalized zero-field critical current density $j_c(T)/j_c(0)$ in Im-$3m$-H_3S sample. The black circles are the experimental data (trapped flux is created at $T_M = 10$ K and $\mu_0 H_M = 3$ T). The dashed blue and green curves correspond to the temperature dependence of critical current density limited by δT_c-type and δl-type pinning; the red dashed curve is the fit of experimental data by the $\delta T_c + \delta l$ model.

conversely accommodated magnetic flux at lower applied magnetic fields and provided a magnetic response before the magnetic flux entered into the massive sample. We expected the true value of H_p and the derived values of λ_L and Ginzburg–Landau parameter $\kappa = \frac{\lambda_L}{\xi}$ to approximately lie between the values observed in the two types of measurement. Using the estimated value of coherence length $\xi(10\text{ K}) \approx 1.85$ nm (ref. [46]), we obtained $\lambda_L(10\text{ K}) \approx 37$ nm (31–40 nm within the estimated limits of h) and $\kappa(10\text{ K}) \approx 20$ (17–22). The corresponding values estimated from the $m(H)$ magnetization measurements[34] were $\lambda_L(0) \approx 22$ nm (18–23 nm) and $\kappa(0) \approx 12$ (10–13).

Critical current density

In addition to the determination of fundamental characteristics T_c and λ_L, we deduced another important characteristic of a superconductor from the measured $m_{\text{trap}}(\mu_0 H_M, T)$ data—the critical current density over a wide temperature range. According to the critical-state Bean model[43,44], a concentric screening current pattern having current density j_c averaged over a sample thickness creates a magnetic moment expressed as $m = \frac{\pi}{3} j_c h \left(\frac{d}{2}\right)^3$.

Thus, the value of $m_{\text{trap}}^s(30\text{ K}) \approx 1.60(1) \times 10^{-8}$ A m² measured in run 1 corresponds to $j_c(30\text{ K}) \approx 7.1(1) \times 10^{10}$ A m⁻². The extrapolation of the experimental data to 0 K for m_{trap}^s (Fig. 3, red dashed curve) provides values of $m_{\text{trap}}^s(0) \approx 1.64(2) \times 10^{-8}$ A m² and $j_c(0) \approx 7.3(1) \times 10^{10}$ A m⁻². The calculated values of j_c in H_3S exceed $j_c(4.2\text{ K})$ in single crystals of iron-based superconductors by two orders of magnitude[47,48] and are approximately two times lower than $j_c(20\text{ K})$ in rare-earth–barium–copper-oxide-coated conductors (second-generation wires) of similar thickness[49].

The ultimate critical current density is limited by the depairing currents[50] as $j_d = \frac{\phi_0}{3\sqrt{3}\pi\mu_0}\frac{1}{\lambda_L^2 \xi}$, where ϕ_0 is the magnetic flux quantum.

Substituting the estimated values of λ_L and ξ, we obtained $j_d \approx 4 \times 10^{13}$ A m⁻². The ratio between $j_c(0)$ and j_d provided additional information. The values of $j_c(0)/j_d$, being approximately in the order of 10^{-2}–10^{-1}, are conventionally observed in low-temperature superconductors, which are characterized by relatively low κ of ~20 and strong pinning that stems from the interaction of vortices with extended defects[51]. However, lower values of $j_c(0)/j_d$ of approximately 10^{-3}–10^{-2} are characteristic for high-temperature superconductors, for example, the cuprate family in which κ is large (of the order of 100) and relatively weaker pinning originates from point defects, such as oxygen vacancies[52]. To improve the in-field critical current performance of cuprates, different types of artificial pinning centre were introduced into the sample structure. The synthesized sample of H_3S was characterized by strong pinning (as discussed below), but the ratio of $j_c(0)/j_d$ was fairly small (of the order of 10^{-3}). This suggested that the density of defect centres in the sintered sample was not the maximum and could be further enhanced, for example, by modifying the synthesis protocol.

The different factors influencing the flux pinning in type-II superconductors are divided into two main types: δT_c and δl (refs. [51,53]). The δl-type pinning arises from a spatial variation in the mean free path of charge carriers, and the defects are small and point sized, for example, hydrogen vacancies in hydrides. The δT_c-type pinning is caused by a spatial variation in κ due to fluctuations in T_c, and the defects are larger than ξ, such as dislocations, grain boundaries and deviations in the chemical composition. Pressure gradients can also cause variations in T_c in the case of samples in DACs. We compared the temperature dependence of the normalized critical current density $j_c(T)/j_c(0)$ in the H_3S sample with the simulated curves for δT_c and δl types of pinning (Fig. 3). Both theoretical curves for pure δT_c and δl types of pinning deviate from the experimental data; however, the resulting fit of the data showed that the δT_c type of pinning dominates over the δl type.

Pinning and thermally activated motion of vortices

The kinetics of m_{trap} demonstrates an extremely slow rate of flux creep even at temperatures in the vicinity of T_c, at which thermal fluctuations must be substantially higher (Fig. 4c). The estimated creep rate $S = \frac{1}{m_{\text{trap,0}}}\frac{dm_{\text{trap}}}{d\ln t}$ in Im-$3m$-H_3S varied from ≈ 0.002 (or 500 ppm h⁻¹) at 165 and 180 K to ≈ 0.005 (or 2,000 ppm h⁻¹) at 185 K, which was comparable with the lowest values of S measured in type-II superconductors[54], including the extremely slow creep rate in high-j_c MgB₂ films at substantially lower $T/T_c < 0.5$ (ref. [55]). The scale of fluctuations responsible for vortex melting[56] and vortex creep[54] in a superconductor can be quantified using the Ginzburg–Levanyuk number as $\text{Gi} = \frac{1}{2}\left(\frac{2\pi\mu_0 k_B T_c \lambda_L^2}{\phi_0^2 \xi}\right)^2$, where k_B is the Boltzmann constant. Here $\text{Gi} \approx 7 \times 10^{-6}$ in H_3S was substantially lower than the values reported for cuprate-based (of the order of 10^{-2}) and iron-based (of the order of 10^{-5}–10^{-2}) high-temperature superconductors[54,56], and comparable with those reported in low-temperature superconductors (10^{-9}–10^{-6}) and MgB₂ (10^{-6}). The observed slow creep rate S in H_3S was close to the theoretical limit demarcated by the approximate $\text{Gi}^{\frac{1}{2}}\frac{T}{T_c}$ line[54] and was in good agreement with the lower values of λ_L and κ (larger values of λ_L would lead to the theoretical limit of S being higher than the observed value). Additionally, electrical transport measurements of Im-$3m$-H_3S at high magnetic fields[46] showed weak vortex fluctuations and narrow vortex liquid regions due to the low values of κ and Gi.

On account of the strong pinning of vortices in the H_3S sample, the amount of the trapped flux solely depended on H_M at which the flux was generated and the maximum temperature at which the sample was exposed after the magnetization step (Fig. 4). For example, m_{trap} created at $\mu_0 H_M = 1$ T by three different protocols merged at 100 K and above on subsequent warming (Fig. 4a, brown and orange curves of cycle II,
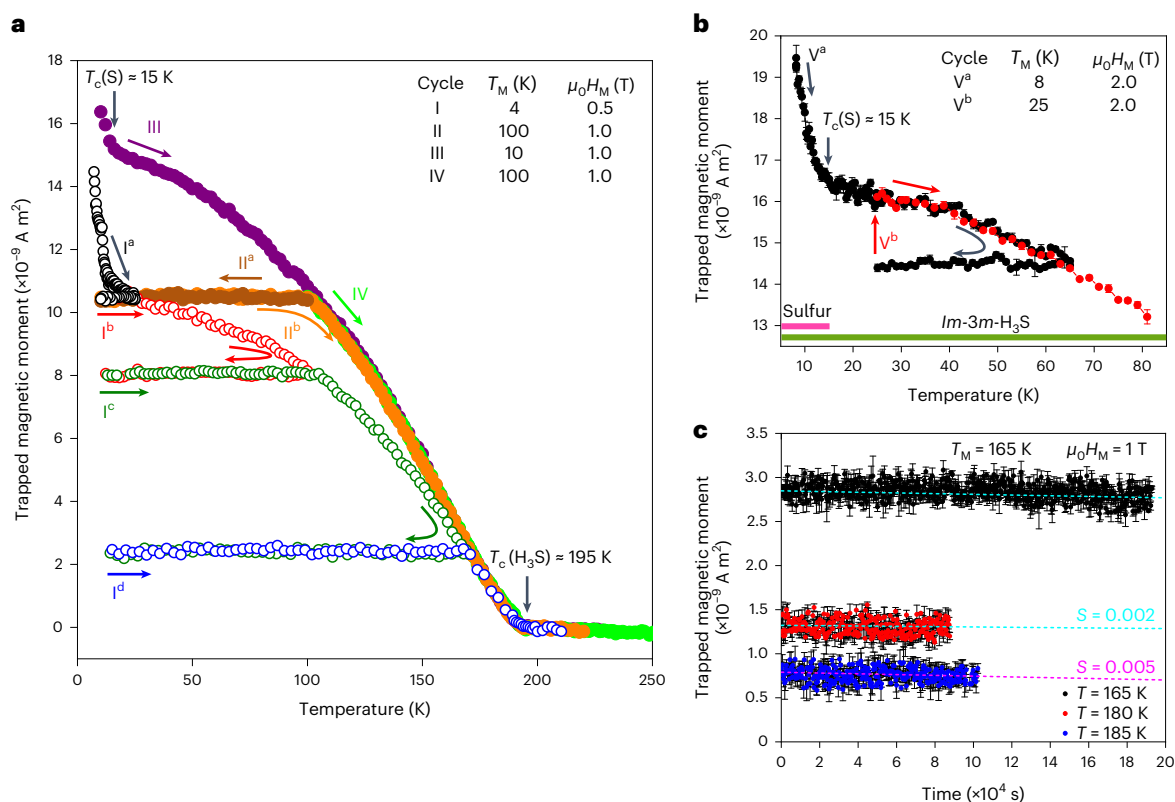
Fig. 4 | Vortex pinning in H$_3$S. a, Temperature dependence of a trapped magnetic moment created at different temperatures T_M and magnetic fields H_M of magnetization. The arrows show the change in temperature in different warming/cooling cycles. **b**, Temperature dependence of a trapped magnetic moment in H$_3$S generated at $\mu_0 H_M = 2$ T and $T_M = 8$ K (black data, cycle V^a).

The trapped flux can be restored if the sample is magnetized again (red data, cycle V^b). **c**, Creep of the trapped flux in H$_3$S at several temperatures near T_c (the trapped flux was generated at $\mu_0 H_M = 1$ T and $T_M = 165$ K). The error bars represent the standard deviation from multiple measurements.

purple curve of cycle III and green curve of cycle IV). The behaviour of m_{trap} was found to be independent of temperature if the sample was warmed to a certain temperature below T_c and cooled down again (Fig. 4a,b shows the horizontal trend of $m_{trap}(T)$). No pronounced hysteresis was observed for the magnetic moment during the cooling/warming cycles. This memory effect, which allows one to control the amount of trapped flux in the superconducting sample, stems from the very strong pinning of the vortices.

Trapped flux in lanthanum superhydrides

The trapped magnetic flux was further probed in the lanthanum–hydrogen system. The ZFC curve of the $m(T)$ data measured at an applied magnetic field of 10 mT demonstrate an extended transition with the onset of $T_c \approx 200$ K at 120 ± 5 GPa (Fig. 5a). The observed T_c was in good agreement with the values of the $C2/m$-LaH$_{10}$ phase at similar pressures measured by electrical transport measurements[57]. The transition at $T_c \approx 200$ K was notably broader than that measured in the initial sample of Fm-3m-LaH$_{10}$ at 130 ± 8 GPa with $T_c \approx 231$ (ref. 34), thus indicating the poorer quality of the superconducting phase. Probably, the high-temperature superconducting Fm-3m-LaH$_{10}$ phase sustained structural distortions into the $C2/m$-LaH$_{10}$ phase and partial decomposition into the hydrogen-deficient phases due to the unexpected drop in pressure during transportation from the synchrotron (Methods).

Contrarily, the trapped flux method demonstrates more pronounced superconducting transitions in this sample (Fig. 5b and Extended Data Fig. 3). In addition to the detection of the transition at ~200 K in the $C2/m$-LaH$_{10}$ phase, it revealed a superconducting state of another phase below ~70 K. Superconductivity with $T_c \approx 70$ K was previously observed in several samples prepared from La and H$_2$ (taken in a

large deficiency) at approximately 150–178 GPa by four-probe electrical transport measurements and could be related to LaH$_x$ (where $3 < x < 10$)[8]. We were unable to perform the full set of measurements of the trapped flux generated at different H_M values as we did for the H$_3$S sample. At magnetization of the sample at $\mu_0 H_M = 4$ T, one of the diamonds cracked, and the pressure dropped below ~10 GPa. However, this allowed us to measure the background response of the DAC body induced after sweeping off a high magnetic field of 4 T. No remnant nonlinear magnetic background of the DAC body or other anomalies in the reference $m_{trap}(T)$ curve were detected at ~10 GPa when the sample was evidently not superconducting (Fig. 5b, cycle III). Furthermore, we clearly demonstrated that the observed superconducting transitions in the $m_{trap}(T)$ data collected at 120 ± 5 GPa (Fig. 5b, cycles I and II) belonged to the sample and not to the high-pressure assembly (DAC, gasket, diamonds and so on).

Discussion

The Meissner effect is one of the most fundamental visualizations of superconductivity and it has been considered as the proof for bulk superconductivity. However, the magnitude of the Meissner effect in type-II superconductors substantially varies in experiments from almost complete expulsion in pinning-free conventional type-II superconductors[58,59] to practically no expulsion in iron pnictides[60] or even to magnetic moment enhancement in various materials with extreme sensitivity to disorder[61–64]. The specific features of the Meissner effect in high-temperature superconductors and its strong suppression by external magnetic fields in the mixed state are associated with the strong pinning, which prevents the vortices inside the sample from shifting towards the sample surface even after crossing the $H_{c1}(T)$ line[65,66]. The subtle or scarcely observable Meissner effect (in the FC mode) in H$_3$S
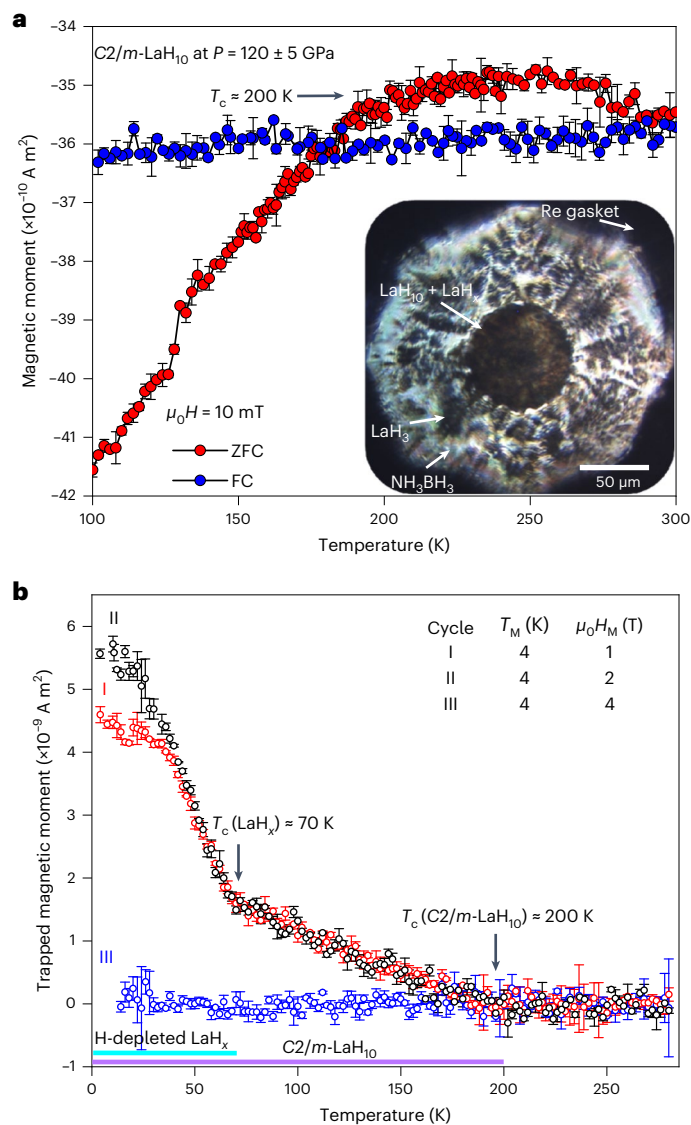
Fig. 5 | Magnetic measurements of sample containing $C2/m$-LaH$_{10}$ and LaH$_x$. **a**, ZFC and FC $m(T)$ data of $C2/m$-LaH$_{10}$ and LaH$_x$ ($3 < x < 10$) at 120 ± 5 GPa. The inset shows a photograph of the sample. **b**, Temperature dependence of a trapped magnetic moment at zero field. The red and black open circles correspond to the temperature dependence of the trapped flux created under ZFC conditions at magnetic fields of $\mu_0 H_M = 1$ and 2 T, respectively. The blue open circles are the data of the same sample at ~10 GPa after magnetization at $\mu_0 H_M = 4$ T, showing the absence of a nonlinear magnetic background from the DAC without the superconducting sample. The error bars represent the standard deviation from multiple measurements.

(ref. 34) agrees with the very strong pinning observed in the present work in H$_3$S even at temperatures near T_c. Under FC conditions, the strong pinning leads to the trapping of magnetic flux in the superconducting H$_3$S already at 0.5 mT, that is, much lower than H_p. Such strong pinning of vortices may also be promoted by the high-pressure conditions. The absence of a pronounced Meissner effect in elemental sulfur and LaH$_{10}$ supports this hypothesis, although the systematic measurements of different high-pressure superconductors are required to prove it.

Standard $m(T)$ and $m(H)$ magnetization measurements at applied magnetic fields, which demonstrate the shielding of external magnetic fields by a sample in the Meissner state, unavoidably yield a large background of the body of the DAC in the registered value of magnetic moment. Therefore, the measured magnetic moment needs to be corrected using the reference measurements either of the same sample above its T_c (refs. 3,29) or of non-superconducting precursors[29,34]. The background subtraction can, however, be difficult if the DAC environment is contaminated by magnetic impurities or if the background becomes disproportionally larger than the response of a superconductor (at higher applied magnetic fields, when the penetration of magnetic flux into a superconductor suppresses the signal from screening Meissner currents).

Importantly, the response from the trapped flux at zero magnetic field was almost not perturbed by the background stemming from the DAC, including diamond anvils and a rhenium gasket. This substantially simplifies the measurements of superconducting samples at high pressures in a SQUID.

Additionally, unlike electrical transport measurements, the trapped flux method is sensitive to a particular superconducting phase in mixtures because it does not require the specific arrangement of different phases relative to electrical leads. The analysis of the $m_{trap}(T)$ data provides estimations for important characteristics of superconductivity, such as H_{c1}, λ_L, pinning of vortices and especially j_c, which can be probed in a wide temperature range. We believe that the trapped flux method, which shows great benefit for high-pressure studies, has also been underestimated for the study of superconductivity at ambient pressure. It can be a powerful tool for the routine screening of new superconducting materials, the study of multiphase, contaminated samples or samples with a low superconducting fraction.

Online content

Any methods, additional references, Nature Portfolio reporting summaries, source data, extended data, supplementary information, acknowledgements, peer review information; details of author contributions and competing interests; and statements of data and code availability are available at https://doi.org/10.1038/s41567-023-02089-1.

References

1. Schilling, A. et al. Superconductivity above 130 K in the Hg–Ba–Ca–Cu–O system. *Nature* **363**, 56–58 (1993).
2. Parkin, S. S. P. et al. Bulk superconductivity at 125 K in Tl$_2$Ca$_2$Ba$_2$Cu$_3$O$_x$. *Phys. Rev. Lett.* **60**, 2539–2542 (1988).
3. Drozdov, A. P. et al. Conventional superconductivity at 203 Kelvin at high pressures in the sulfur hydride system. *Nature* **525**, 73–76 (2015).
4. Bardeen, J. et al. Theory of superconductivity. *Phys. Rev.* **108**, 1175–1204 (1957).
5. Eliashberg, G. Interactions between electrons and lattice vibrations in a superconductor. *Sov. Phys. JETP* **11**, 696–702 (1960).
6. Migdal, A. Interaction between electrons and lattice vibrations in a normal metal. *Sov. Phys. JETP* **7**, 996–1001 (1958).
7. Kong, P. et al. Superconductivity up to 243 K in the yttrium-hydrogen system under high pressure. *Nat. Commun.* **12**, 5075 (2021).
8. Drozdov, A. P. et al. Superconductivity at 250 K in lanthanum hydride under high pressures. *Nature* **569**, 528–531 (2019).
9. Somayazulu, M. et al. Evidence for superconductivity above 260 K in lanthanum superhydride at megabar pressures. *Phys. Rev. Lett.* **122**, 027001 (2019).
10. Hong, F. et al. Superconductivity of lanthanum superhydride investigated using the standard four-probe configuration under high pressures. *Chinese Phys. Lett.* **37**, 107401 (2020).
11. Duan, D. et al. Pressure-induced metallization of dense (H$_2$S)$_2$H$_2$ with high-T_c superconductivity. *Sci. Rep.* **4**, 6968 (2014).
12. Liu, H. et al. Potential high-T_c superconducting lanthanum and yttrium hydrides at high pressure. *Proc. Natl Acad. Sci. USA* **114**, 6990–6995 (2017).
13. Peng, F. et al. Hydrogen clathrate structures in rare earth hydrides at high pressures: possible route to room-temperature superconductivity. *Phys. Rev. Lett.* **119**, 107001 (2017).

14. Flores-Livas, J. A. et al. A perspective on conventional high-temperature superconductors at high pressure: methods and materials. *Phys. Rep.* **856**, 1–78 (2020).

15. Boeri, L. et al. The 2021 room-temperature superconductivity roadmap. *J. Phys.: Condens. Matter* **34**, 183002 (2022).

16. Pickard, C. J. et al. Superconducting hydrides under pressure. *Annu. Rev. Condens. Matter Phys.* **11**, 57–76 (2020).

17. Zhong, X. et al. Prediction of above-room-temperature superconductivity in lanthanide/actinide extreme superhydrides. *J. Am. Chem. Soc.* **144**, 13394–13400 (2022).

18. Sun, Y. et al. Route to a superconducting phase above room temperature in electron-doped hydride compounds under high pressure. *Phys. Rev. Lett.* **123**, 097001 (2019).

19. Lucrezi, R. et al. In-silico synthesis of lowest-pressure high-T_c ternary superhydrides. *npj Comput. Mater.* **8**, 119 (2022).

20. Di Cataldo, S. et al. LaBH$_8$: towards high-T_c low-pressure superconductivity in ternary superhydrides. *Phys. Rev. B* **104**, L020511 (2021).

21. Bi, J. et al. Giant enhancement of superconducting critical temperature in substitutional alloy (La,Ce)H$_9$. *Nat. Commun.* **13**, 5952 (2022).

22. Semenok, D. V. et al. Superconductivity at 253 K in lanthanum–yttrium ternary hydrides. *Mater. Today* **48**, 18–28 (2021).

23. Semenok, D. V. et al. Effect of magnetic impurities on superconductivity in LaH$_{10}$. *Adv. Mater.* **34**, 2204038 (2022).

24. Chen, W. et al. Enhancement of superconducting properties in the La–Ce–H system at moderate pressures. *Nat. Commun.* **14**, 2660 (2023).

25. Schilling, J. S. Studies in superconductivity at extreme pressures. *Phys. C* **460–462**, 182–185 (2007).

26. Hamlin, J. J. Superconductivity in the metallic elements at high pressures. *Phys. C* **514**, 59–76 (2015).

27. Shimizu, K. Superconductivity from insulating elements under high pressure. *Phys. C* **514**, 46–49 (2015).

28. Timofeev, Y. A. Detection of superconductivity in high-pressure diamond anvil cell by magnetic susceptibility technique. *Prib. Tekh. Eksper.* **5**, 186–189 (1992).

29. Eremets, M. I. et al. High-temperature superconductivity in hydrides: experimental evidence and details. *J. Supercond. Nov. Magn.* **35**, 965–977 (2022).

30. Struzhkin, V. V. et al. Superconductivity at 10–17 K in compressed sulphur. *Nature* **390**, 382–384 (1997).

31. Struzhkin, V. et al. Superconductivity in La and Y hydrides: remaining questions to experiment and theory. *Matter Radiat. Extrem.* **5**, 028201 (2020).

32. Alireza, P. L. & Lonzarich, G. G. Miniature anvil cell for high-pressure measurements in a commercial superconducting quantum interference device magnetometer. *Rev. Sci. Instrum.* **80**, 023906 (2009).

33. Marizy, A. et al. A symmetric miniature diamond anvil cell for magnetic measurements on dense hydrides in a SQUID magnetometer. *High. Press. Res.* **37**, 465–474 (2017).

34. Minkov, V. S. et al. Magnetic field screening in hydrogen-rich high-temperature superconductors. *Nat. Commun.* **13**, 3194 (2022).

35. Yakovlev, E. N. et al. Superconductivity of sulfur at high-pressures. *JETP Lett.* **28**, 340–342 (1978).

36. Kometani, S. et al. Observation of pressure-induced superconductivity of sulfur. *J. Phys. Soc. Jpn* **66**, 2564–2565 (1997).

37. Treimer, W. et al. Polarized neutron imaging and three-dimensional calculation of magnetic flux trapping in bulk of superconductors. *Phys. Rev. B* **85**, 184522 (2012).

38. Dhiman, I. et al. Role of temperature on flux trap behavior in <100> Pb cylindrical sample: polarized neutron radiography investigation. *Phys. Procedia* **69**, 420–426 (2015).

39. Altshuler, E. et al. Flux trapping in transport measurements of YBa$_2$Cu$_3$O$_{7-x}$ superconductors. *Phys. C* **177**, 61–66 (1991).

40. Buntar, V. et al. Lower critical fields of alkali-metal-doped fullerene superconductors. *Phys. Rev. B* **54**, R9651–R9654 (1996).

41. Buntar, V. & Weber, H. W. Magnetic properties of fullerene superconductors. *Supercond. Sci. Technol.* **9**, 599–615 (1996).

42. Müller, K. H. et al. Connectivity and limitation of critical current in Bi-Pb-Sr-Ca-Cu/Ag tapes. *Phys. Rev. B* **60**, 659–666 (1999).

43. Bean, C. P. Magnetization of hard superconductors. *Phys. Rev. Lett.* **8**, 250–253 (1962).

44. Bean, C. P. Magnetization of high-field superconductors. *Rev. Mod. Phys.* **36**, 31–39 (1964).

45. Moshchalkov, V. V. et al. Anisotropy of the first critical field and critical current in YBa$_2$Cu$_3$O$_{6.9}$ single crystals. *Phys. C* **175**, 407–418 (1991).

46. Mozaffari, S. et al. Superconducting phase diagram of H$_3$S under high magnetic fields. *Nat. Commun.* **10**, 2522 (2019).

47. Yamamoto, A. et al. Small anisotropy, weak thermal fluctuations, and high field superconductivity in Co-doped iron pnictide Ba(Fe$_{1-x}$Co$_x$)$_2$As$_2$. *Appl. Phys. Lett.* **94**, 062511 (2009).

48. Sun, Y. et al. Deviation from canonical collective creep behavior in Li$_{0.8}$Fe$_{0.2}$OHFeSe. *J. Phys. Soc. Jpn* **88**, 034703 (2019).

49. Molodyk, A. et al. Development and large volume production of extremely high current density YBa$_2$Cu$_3$O$_7$ superconducting wires for fusion. *Sci. Rep.* **11**, 2084 (2021).

50. Griessen, R. et al. Evidence for mean free path fluctuation induced pinning in YBa$_2$Cu$_3$O$_7$ and YBa$_2$Cu$_4$O$_8$ films. *Phys. Rev. Lett.* **72**, 1910–1913 (1994).

51. Blatter, G. et al. Vortices in high-temperature superconductors. *Rev. Mod. Phys.* **66**, 1125–1388 (1994).

52. Van Gennep, D. et al. Sharp peak of the critical current density in BaFe$_{2-x}$Ni$_x$As$_2$ at optimal composition. *Phys. Rev. B* **101**, 235163 (2020).

53. Dew-Hughes, D. Flux pinning mechanisms in type II superconductors. *Philos. Mag.* **30**, 293–305 (1974).

54. Eley, S. et al. Universal lower limit on vortex creep in superconductors. *Nat. Mater.* **16**, 409–413 (2017).

55. Thompson, J. R. et al. Vortex pinning and slow creep in high-J_c MgB$_2$ thin films: a magnetic and transport study. *Supercond. Sci. Technol.* **18**, 970–976 (2005).

56. Koshelev, A. E. et al. Melting of vortex lattice in the magnetic superconductor RbEuFe$_4$As$_4$. *Phys. Rev. B* **100**, 094518 (2019).

57. Sun, D. et al. High-temperature superconductivity on the verge of a structural instability in lanthanum superhydride. *Nat. Commun.* **12**, 6863 (2021).

58. Huebener, R. *Magnetic Flux Structures of Superconductors* (Springer, 2001).

59. Poole, C. P. J. et al. *Superconductivity* 3rd edn, 870 (Elsevier, 2014).

60. Prozorov, R. et al. Anomalous Meissner effect in pnictide superconductors. *Phys. Rev. B* **82**, 180513 (2010).

61. Braunisch, W. et al. Paramagnetic Meissner effect in Bi high-temperature superconductors. *Phys. Rev. Lett.* **68**, 1908–1911 (1992).

62. Braunisch, W. et al. Paramagnetic Meissner effect in high-temperature superconductors. *Phys. Rev. B* **48**, 4030–4042 (1993).

63. Thompson, D. J. et al. Observation of paramagnetic Meissner effect in niobium disks. *Phys. Rev. Lett.* **75**, 529–532 (1995).

64. Geim, A. K. et al. Paramagnetic Meissner effect in small superconductors. *Nature* **396**, 144–146 (1998).

65. Tomioka, Y. et al. The Meissner and shielding effects in niobium in relation to oxide superconductors. *Phys. C* **215**, 297–304 (1993).

66. Moshchalkov, V. V. & Zhukov, A. A. The Meissner effect in superconductors with strong vortex pinning. *Phys. B* **169**, 601–602 (1991).

Methods

Samples

We used the same samples that were studied in our previous work[34]. The superconducting Im-$3m$-H_3S and Fm-$3m$-LaH_{10} phases were synthesized from sandwiched S + NH_3BH_3 and LaH_3 + NH_3BH_3 samples pressurized in miniature DACs, which were specially designed for a standard commercial SQUID magnetometer[3,34].

Sulfur (99.999%, Alfa), NH_3BH_3 (97.000%, Sigma-Aldrich) and LaH_3 (synthesized from La (99.900%, Alfa Aesar) and H_2 (99.999%, Spectra Gases)) were used as the initial reactants. The loading of samples into the DACs was handled in an inert Ar atmosphere with residual O_2 and H_2O contents of <0.1 ppm. NH_3BH_3 acted both as a source of H_2 and a thermal isolator from the diamonds during laser heating. The thin plates of S, LaH_3 and NH_3BH_3 for the sandwiched samples were moulded out from the corresponding powder samples by squeezing them between two large 1-mm-diameter diamond anvils. The thickness of the plates was monitored by the interference of visible light.

The sandwiched samples, in which 8-μm-thick S or 6-μm-thick LaH_3 plates were interposed between two ~10–15-μm-thick layers of NH_3BH_3 were put in the hole of pre-indented metallic gaskets. Then, these samples were pressurized to ≈ 167 GPa with a pressure gradient across the culet of about ±7 GPa. The decomposition of NH_3BH_3 and the synthesis of superconducting Im-$3m$-H_3S and Fm-$3m$-LaH_{10} phases were performed using one-side heating with a Nd:YAG pulse laser (wavelength, λ = 1.064 μm; pulse duration, 3 μs; frequency, 10^4 Hz). We heated the samples by horizontally and vertically traversing the ≈ 5-μm-diameter laser spot across the diamond culets. The pressure was estimated using the universal diamond edge Raman scale[67]. Further details of the preparation of DACs, chemical synthesis of samples, estimation of pressure values and characterization of the initial reactants and final products are available elsewhere[34].

The DAC with the Im-$3m$-H_3S sample retained the same pressure value of P = 155 ± 5 GPa throughout the measurements, whereas the DAC with the Fm-$3m$-LaH_{10} sample did not survive the transportation from the Advanced Photon Source synchrotron. The pressure decreased from P = 130 ± 8 GPa to P = 120 ± 5 GPa. We attempted to restore the sample and pressurized the DAC to P = 125 ± 5 GPa and heated the sample to ~2,000 K by a pulsed YAG laser. However, the sample demonstrated lower T_c ≈ 200 K and probably corresponded to the structurally distorted $C2/m$ phase of LaH_{10}, which formed from Fm-$3m$-LaH_{10} on decompression at pressures below ≈ 130 GPa (ref. 57). One of the diamond anvils cracked, and the pressure dropped to ~10 GPa during the magnetization step at $\mu_0 H_M$ = 4 T after two successful measurements of the trapped flux generated at 1 and 2 T. The subsequent measurements of the DAC with the decomposed non-superconducting sample magnetized at $\mu_0 H_M$ = 4 T demonstrated the linear background signal of the DAC with no anomalies in the $m_{trap}(T)$ curve over the entire temperature range of 10–280 K.

Magnetization measurements

Magnetization measurements $m(T)$ were performed using the S700X SQUID magnetometer (Cryogenic), and a miniature DAC was attached to a 140-mm-long straw made of a Kapton polyimide film, which was specially designed to minimize the end effects. The position of the sample relative to the pickup coil of the SQUID magnetometer was determined using the ferromagnetic signal from a small steel piece with a size of approximately 140 × 100 × 25 $μm^3$ directly attached to the rhenium gasket surrounding the sample. The steel piece was removed after the centring procedure. The accuracy of sample positioning is approximately ±0.2 mm. The superconducting transition in H_3S and LaH_{10} was probed by ZFC and FC $m(T)$ measurements at 4 and 10 mT, respectively. Here T_c ≈ 195 K in the Im-$3m$-H_3S phase, which was determined as the offset of the diamagnetic transition on the ZFC curves of $m(T)$, was in good agreement with the values estimated in our previous measurements[34]. The much broader superconducting transition in the sample with LaH_{10} and the lower T_c (≈ 200 K) indicated the deterioration

of the superconducting phase of LaH_{10} after altering the pressure in the DAC, which probably sustained the monoclinic structural distortions[57].

The trapped flux was generated in two different protocols under ZFC (run 1) and FC (run 2) conditions. The typical ZFC protocol included cooling of the sample at zero field from $T > T_c$ to the desired temperature T_M below the corresponding T_c, namely, T_M = 10 K for the Im-$3m$-H_3S sample and at T_M = 4 K for the $C2/m$-LaH_{10} sample. Additional experiments were performed where the magnetic flux was trapped in H_3S at T_M = 4 K in cycle I, T_M = 100 K in cycles II and IV and T_M = 8 and 25 K in cycles V[a] and V[b]. A typical magnetization cycle in the ZFC mode consisted of a gradual increase in the applied magnetic field H_M perpendicular to the sample surface at the lowest temperature point T_M, standing at the target value of H_M for an hour, and a gradual decrease in the magnetic field to 0 T. In the FC mode, the sample was cooled from its normal state ($T > T_c$) at the applied magnetic field H_M to the target temperature $T_M < T_c$. Then, H_M was gradually decreased to 0 T. After removing the applied magnetic field H_M in both ZFC and FC modes, the SQUID magnetometer was allowed to stand at 0 T for approximately 5 h to prevent successive measurements of $m_{trap}(T)$ from outliers associated with jumps of flux in the SQUID superconducting magnet. Magnetization flux density $\mu_0 H_M$ ranged from 0.5 mT to 6 T. The $m_{trap}(T)$ measurements were performed on warming (cooling) of the sample with a temperature step of 0.3–3.0 K (a smaller step in the vicinity of T_c) and 3–4 iterations at each temperature point. Additionally, the reference $m_{trap}(T)$ data were measured for the Im-$3m$-H_3S sample by skipping the magnetization cycle ($\mu_0 H_M$ = 0 T). The trapped magnetic moment was determined as the difference between the measured magnetic moment after the magnetization cycle and the residual magnetic moment, which arose from the body of the miniature DAC above the corresponding T_c (Extended data Figs. 1–3). Before each cycle of magnetization, the sample was converted to the normal state by warming to ambient temperature, and the superconducting magnet of the SQUID was degaussed to eliminate the remaining fields.

Measurements of the trapped flux created in the sample of H_3S in runs 1 and 2 were separated in a time of ~6 months. The small discrepancy in the value of m_{trap}^s between the two runs probably arose from the slightly different positions of the superconducting sample relative to the pickup coil of the SQUID magnetometer, which were found at the centring procedure, and not from the different conditions of the creation of the trapped flux (FC or ZFC). Experimental facts that the same values of m_{trap}^s were measured in run 1 under ZFC (2, 3 and 6 T) and FC (4 T) conditions support this explanation.

To determine the background magnetic response of the DAC environment, we released the pressure in the DAC with the superconducting Im-$3m$-H_3S phase down to the atmospheric pressure, that is, transformed the sample into a non-superconducting state and keeping the rest of the DAC environment intact. The released DAC was magnetized following the typical protocol for generating a trapped flux under ZFC and FC conditions at $\mu_0 H_M$ = 2 T, that is, above $\mu_0 H^*$ when the magnetic response of the trapped flux was the maximum. Both ZFC and FC $m(T)$ dependencies revealed the quasi-linear behaviour without anomalies (Extended Data Figs. 1 and 2). Thus, the trapped flux observed for the same DAC with the Im-$3m$-H_3S phase at P = 155 ± 5 GPa before decompression belongs to the superconducting phase and not to the DAC environment.

Estimation of sample size and demagnetization correction

The diameter and thickness of the thin disc-shaped Im-$3m$-H_3S sample were estimated from optical microscopy and X-ray diffraction data as ≈ 85.0 and ≈ 2.8 μm, respectively (theoretical lower and upper limits of h were ≈ 2.1 and ≈ 3.1 μm, respectively). Only the geometry of the ideal disc-shaped sample yielded high values of demagnetization correction ($\frac{1}{1-N}$) of ≈ 20 using the proposed equation for the effective demagnetization factor in another work[68]. However, the real shape of the sample can deviate from the ideal disc, for example, the alteration of the thickness and not perfectly rounded edge of the sample, and

that leads to a decrease in the demagnetization factor. Therefore, we further considered the absolute value of Δm, the difference in $m(T)$ between a normal metal state (above T_c) and a superconducting state (below T_c), which includes geometrical imperfections in the sample shape. This approach gives more reasonable and reliable values of the demagnetization correction as $\frac{1}{1-N} \approx 8.5$ (-7.7–11.4 for the estimated limits of h), which we use for the estimation of H_{c1} (ref. 34).

Data availability
Source data are provided with this paper.

References
67. Eremets, M. I. et al. Universal diamond edge Raman scale to 0.5 terapascal and implications for the metallization of hydrogen. *Nat. Commun.* **14**, 907 (2023).
68. Prozorov, R. & Kogan, V. G. Effective demagnetizing factors of diamagnetic samples of various shapes. *Phys. Rev. Appl.* **10**, 014030 (2018).

Acknowledgements

Author contributions
V.S.M., V.K. and M.I.E. designed the research. M.I.E. designed the miniature DAC. V.S.M. prepared the samples and performed the measurements. V.S.M., V.K., S.L.B. and E.F.T. processed and analysed the data. V.S.M. and M.I.E. wrote the manuscript with input from all co-authors.

Funding

Competing interests
The authors declare no competing interests.

Additional information
Extended data is available for this paper at https://doi.org/10.1038/s41567-023-02089-1.

Supplementary information The online version contains supplementary material available at https://doi.org/10.1038/s41567-023-02089-1.

Correspondence and requests for materials should be addressed to V. S. Minkov or M. I. Eremets.

Peer review information *Nature Physics* thanks Ho-Kwang Mao and the other, anonymous, reviewer(s) for their contribution to the peer review of this work.

Reprints and permissions information is available at www.nature.com/reprints.
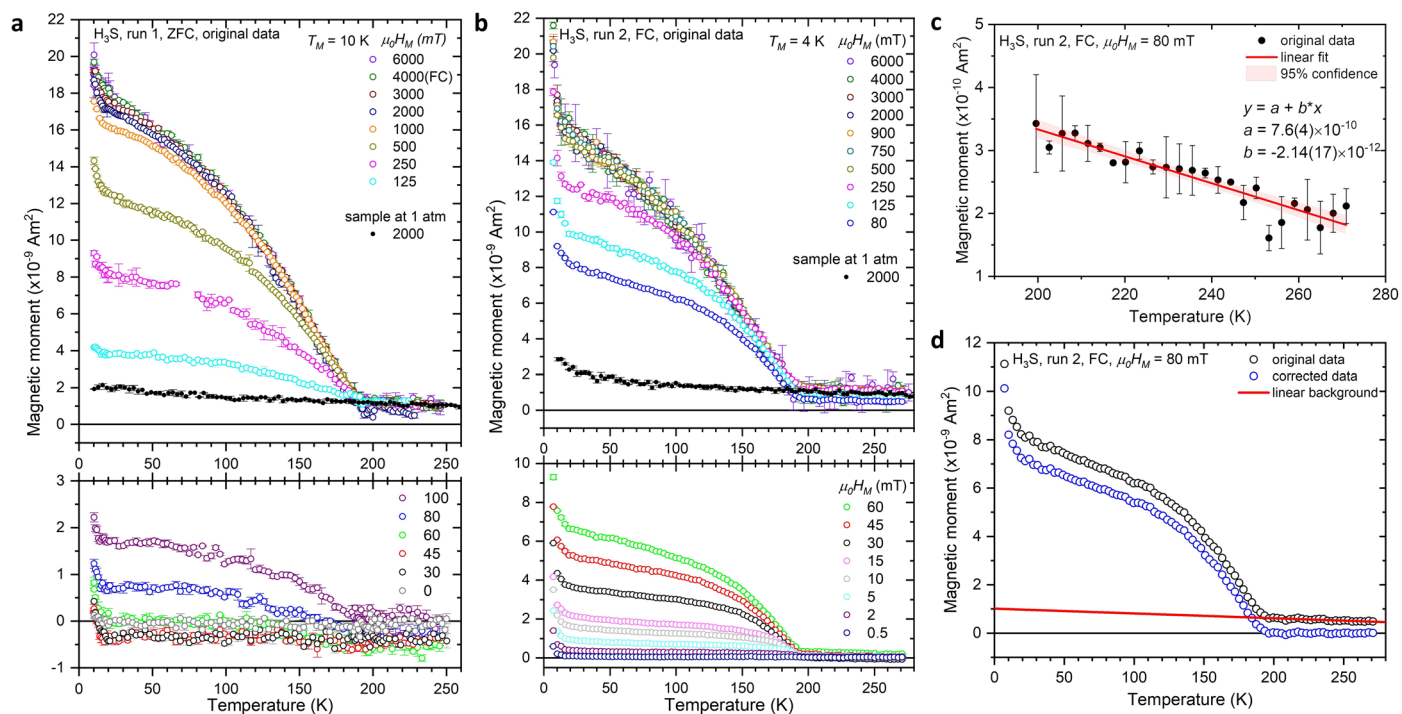
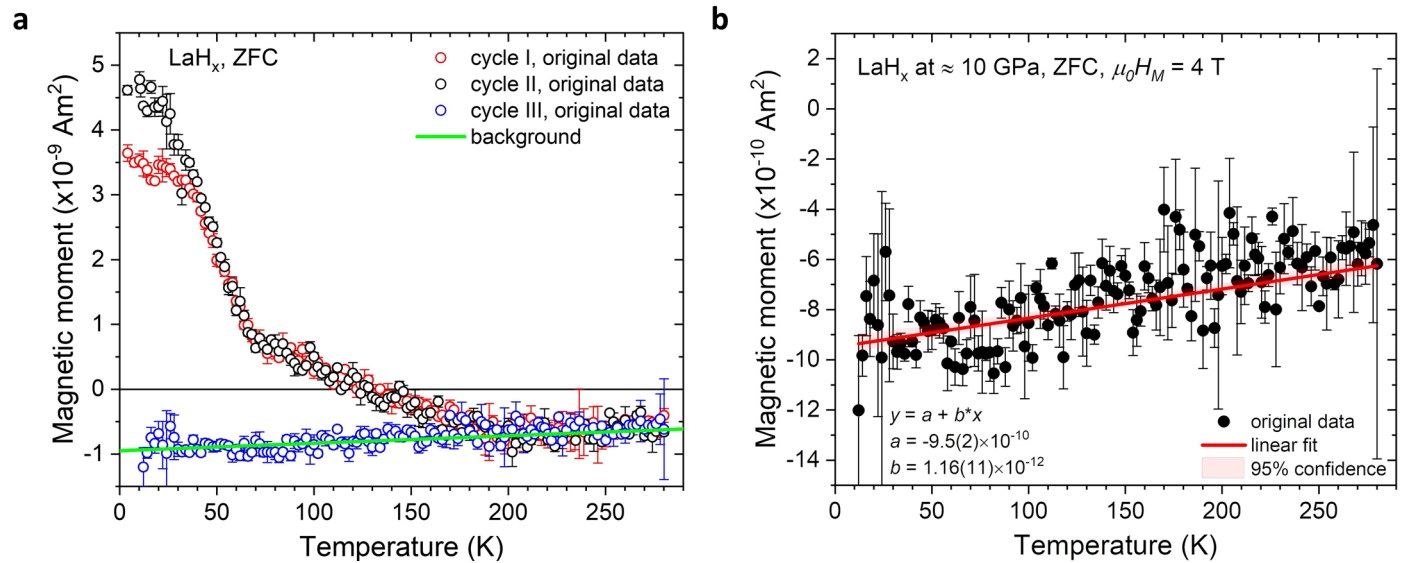**Extended Data Fig. 1 | Raw temperature-dependent data of the trapped flux in the sample containing *Im-3m*-H$_3$S and subtraction of the background.** **a**) and **b**) Raw data of *m(T)* measured for *Im-3m*-H$_3$S sample in run 1 (ZFC) and 2 (FC), respectively. Reference ZFC and FC *m(T)* data measured from the same DAC with the apparent non-superconducting sample after release of pressure down to atmospheric are shown as solid black circles. **c**) The linear fit of the data above T_c (red line) was defined as the background of the corresponding

measurement. **d**) Example of the background subtraction for determination of the trapped magnetic moment in the superconducting sample. Black circles, red line and green circles correspond to original raw data, extrapolated linear background, and corrected $m_{trap}(T)$ for sample of H$_3$S measured in run 2 at $\mu_0 H_M$ = 80 mT. Error bars represent the standard deviation in multiple measurements.
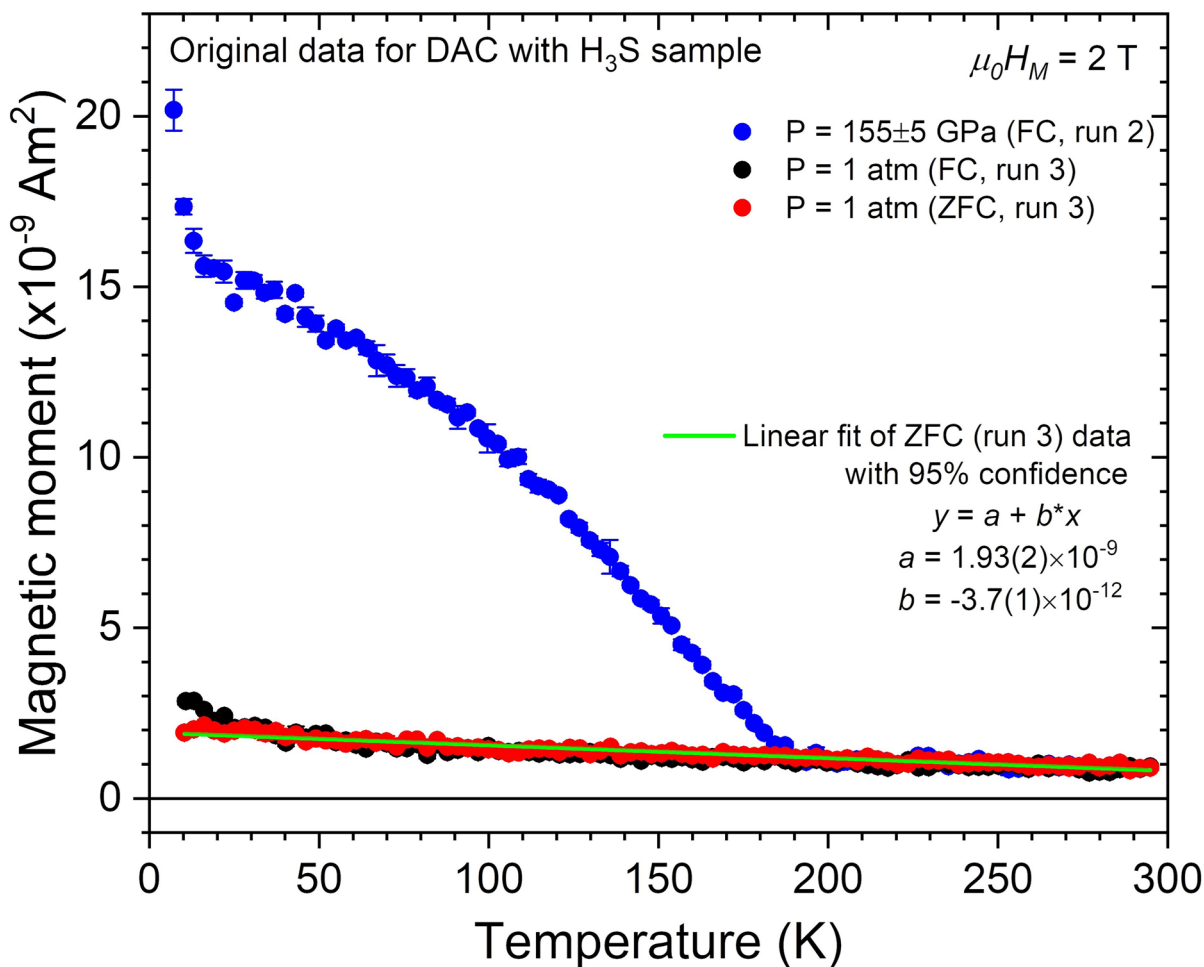
Extended Data Fig. 2 | Background $m(T)$ data for the DAC with the $Im\text{-}3m$-H_3S phase after release of pressure down to atmospheric (run 3), i.e. when the sample decomposed and became non-superconducting. Background $m(T)$ data for the DAC with the $Im\text{-}3m$-H_3S phase after release of pressure down to atmospheric (run 3), that is when sample decomposed and became non-superconducting. Black and red circles correspond to the raw $m(T)$ data measured for the DAC with the sample at 1 atmosphere, which was magnetized at $\mu_0 H_M = 2$ T following the typical protocol for generating of trapped flux under FC and ZFC conditions, respectively. Blue circles correspond to the raw $m(T)$ data measured for the same sample at $P = 155 \pm 5$ GPa before decompression (run 2, FC, $\mu_0 H_M = 2$ T) for comparison. Green line shows the linear fit of the reference ZFC data within 95% confidence. Error bars represent the standard deviation in multiple measurements.

a

b

Extended Data Fig. 3 | Subtraction of the background in raw temperature-dependent data of the trapped flux in sample containing $C2/m$-LaH$_{10}$.
a) Raw data of $m(T)$ measured for sample with LaH$_{10}$. The trapped flux was generated under ZFC conditions at T_M = 4 K and $\mu_0 H_M$ = 1 T and 2 T (red and black circles, respectively). **b**) The background was defined as a linear fit of

the $m(T)$ data obtained for the evidently non-superconducting sample in DAC at ≈10 GPa, which was magnetized under ZFC conditions at $\mu_0 H_M$ = 4 T after the decrease of pressure (blue circles). Error bars represent the standard deviation in multiple measurements.